Multi-scale modelling of pulsed nanosecond dielectric barrier plasma discharges in plane-to-plane geometry

2013 J. Phys. D: Appl. Phys. 46 155205

(http://iopscience.iop.org/0022-3727/46/15/155205)

IOP PUBLISHING JOURNAL OF PHYSICS D: APPLIED PHYSICS

J. Phys. D: Appl. Phys. **46** (2013) 155205 (13pp) doi:10.1088/0022-3727/46/15/155205

Multi-scale modelling of pulsed nanosecond dielectric barrier plasma discharges in plane-to-plane geometry

Sharath Nagaraja[1], **Vigor Yang**[1] **and Igor Adamovich**[2]

[1] School of Aerospace Engineering, Georgia Institute of Technology, Atlanta, GA 30332, USA
[2] Department of Mechanical and Aerospace Engineering, Ohio State University, Columbus, OH 43210, USA

E-mail: vigor.yang@aerospace.gatech.edu and Adamovich.1@osu.edu

Received 5 January 2013, in final form 20 February 2013
Published 22 March 2013
Online at stacks.iop.org/JPhysD/46/155205

Abstract

An integrated theoretical and numerical framework is developed to study the dynamics of energy coupling, gas heating and generation of active species by repetitively pulsed nanosecond dielectric barrier discharges (NS DBDs) in air. The work represents one of the first attempts to simulate, in a self-consistent manner, multiple (more than 100) nanosecond pulses. Detailed information is obtained about the electric-field transients during each voltage pulse, and accumulation of plasma generated species and gas heating over ms timescales. The plasma is modelled using a two-temperature, detailed chemistry scheme, with ions and neutral species in thermal equilibrium at the gas temperature, and electrons in thermal nonequilibrium. The analysis is conducted with pressures and pulsing frequency in the range 40–100 Torr and 1–10^5 Hz, respectively. The input electrical energy is directly proportional to the number density, and remains fairly constant on a per molecule basis from pulse to pulse. Repetitive pulsing results in uniform production of atomic oxygen in the discharge volume via electron-impact dissociation during voltage pulses, and through quenching of excited nitrogen molecules in the afterglow. The ion Joule effect causes rapid gas heating of ~40 K/pulse in the cathode sheath and generates weak acoustic waves. Conductive heat loss to the walls during the time interval between voltage pulses prevents overheating of the cathode layer and development of ionization instabilities. A uniform 'hat-shaped' temperature profile develops in the discharge volume after multiple pulses, due to chemical heat release from quenching of excited species. This finding may explain experimentally observed volumetric ignition (as opposed to hot-spot ignition) in fuel–air mixtures subject to NS DBD.

(Some figures may appear in colour only in the online journal)

1. Introduction

In plasma discharges, the electrons gain energy through an external electric field, and lose via elastic and inelastic collisions with gas molecules [1]. The large difference of mass between electrons and gas species makes elastic collisions inefficient, and the rate of transfer of electron energy to translational degrees of freedom of the gas is slow. On the other hand, inelastic collisions of high energy electrons with gas molecules cause rapid excitation of internal energy modes as well as dissociation and ionization. The reduced electric field, E/N (ratio of electric field to gas number density) is a critical parameter governing the electron energy. Depending on the E/N value, the plasma physics and chemistry can be vastly different.

Application of high-voltage (several times the breakdown threshold) nanosecond pulses results in a strongly nonequilibrium plasma with uniform ionization and excitation in the discharge volume [2]. The short pulse duration (10–100 ns) significantly improves plasma stability and prevents glow to arc transition, since it is much shorter than characteristic timescales for development of ionization instabilities [2]. The

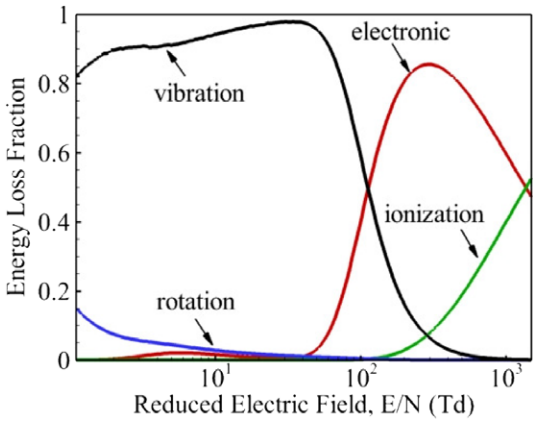

Figure 1. Fraction of electron energy lost in excitation of internal energy modes and ionization of O_2 and N_2 molecules in air as a function of reduced electric field, E/N.

nanosecond plasma discharges have been recently studied for a wide variety of applications such as enhancement of ignition and combustion [1–7], high speed flow control [8], jet noise reduction [9], sterilization and other biomedical applications [10–12]. In a nonequilibrium discharge, the electron energy distribution function (EEDF) deviates significantly from an equilibrium Maxwellian distribution, with the mean electron temperature being several times greater than the gas temperature [1]. Several open-source codes such as BOLSIG [13] are available to calculate the EEDF by solving the Boltzmann equation. Electron-impact elastic and inelastic collision cross-sections are used as input data. The nonequilibrium EEDF is approximated by a two-term expansion and assumed to be a function of only the local electric-field value.

Figure 1 shows a sample result of a BOLSIG calculation for air (79% N_2 and 21% O_2) at 300 K. The fraction of input electrical power consumed in electron-impact excitation and ionization is obtained as a function of E/N. Rotational excitation is the major channel for electron energy transfer at $E/N < 1$ Td. The excited levels rapidly relax to create a high-temperature equilibrium plasma. For E/N between 1 and 100 Td, electrons have sufficient kinetic energy to excite progressively higher vibrational levels of air molecules. The average vibrational temperature can be significantly higher than the translational counterpart, with substantial nonequilibrium among the vibrational levels as well. Vibrational relaxation in air plasma is controlled primarily by the density of O atoms [14]. The relaxation time has been measured to be 20–30 ms after a burst of nanosecond pulse discharges in plane-to-plane geometry at 100 Torr [14]. This is much slower compared with discharge pulse duration (∼50 ns), and time interval between the pulses (10–100 μs). Excitation of singlet states of oxygen ($O_2(a^1)$, $O_2(b^1)$) and triplet states of nitrogen ($N_2(A^3)$, $N_2(B^3)$, $N_2(C^3)$) consumes a major fraction of electron energy when E/N is in the range 100–1000 Td, with a small portion used in dissociation of O_2 molecules. Ionization becomes progressively important for $E/N > 500$ Td, and dominates over all other energy modes beyond 1000 Td. It must be noted that the results in figure 1 are valid when the applied field varies at a rate

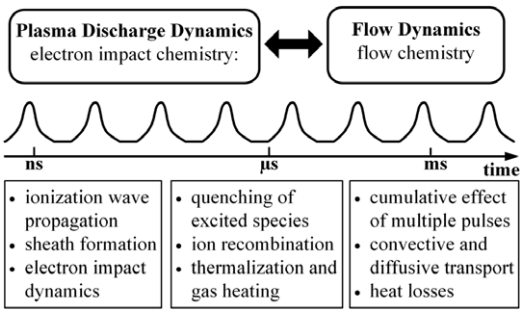

Figure 2. Disparity in timescales of different physical phenomena for flow and repetitively pulsed nanosecond plasma interactions.

slower than the relaxation of the EEDF [15]. Under the present conditions (40–100 Torr and 300–600 K), the electron–neutral collision frequency is $\nu_{en} \sim N v_e \sigma_{en} \sim 10^{12}\ s^{-1}$, where $N \sim 3 \times 10^{18}\ cm^{-3}$ is the number density, $v_e \sim 10^8\ cm\ s^{-1}$ the random thermal velocity of electrons with average energy of ∼1 eV, and $\sigma_{en} \sim 3 \times 10^{15}\ cm^2$ the transport cross-section. Thus, the EEDF relaxation time, $\tau_{en} \sim 1/\nu_{en} \sim 10^{-12}$ s, is much shorter compared with the characteristic time for applied voltage change, $\tau_{pulse} \sim 10^{-8}$ s (see figure 4(*b*)).

Several numerical investigations of nanosecond discharges have been conducted with different levels of details [16–19]. Macheret *et al* [16] performed one-dimensional (1D) simulations of plasma generated by a trapezoidal pulse (2 ns duration and 10 kV peak voltage) in a plane-to-plane geometry. The energy cost of ionization and electric-field dynamics was analysed using a hydrodynamic model with three species (positive ion, negative ion and electron). Pancheshnyi *et al* [17] reported 2D simulations of cathode directed streamer discharge in a pin-to-plane geometry. Only electrons and charged species reactions were included in the kinetics scheme, since the focus of the study was on small timescale transients (up to 100 ns). Unfer and Boeuf [18] developed a 2D model to study the interaction of flow over a flat plate with a surface barrier nanosecond discharge in air. The simulations were conducted with two species (positive ion and electron) for a 35 ns trapezoidal voltage pulse. Fast gas heating and formation of compression waves were investigated making use of a simple phenomenological model for the thermalization process. Recently, Poggie *et al* [19] carried out 1D simulation of nanosecond dielectric barrier discharges (NS DBDs) in a plane-to-plane geometry, with consideration of realistic air-plasma kinetics (23 species 50 reactions) and compressible flow motions. A 24 ns Gaussian voltage pulse caused breakdown in the discharge volume transforming the input electrical energy to various chemical energy modes (ionization, dissociation and excitation). The simulation was continued up to 10 μs to study the quenching of excited species and generation of compression waves.

No attempt, however, has been made so far to treat multiple nanosecond voltage pulses with detailed chemical kinetics. The multi-scale nature of the problem offers enormous challenges in maintaining numerical resolution, accuracy and stability. The wide disparity in timescales between different physical phenomena is illustrated in figure 2. Electron-impact reactions generate ions and excited species during a high-voltage nanosecond pulse. The sheath layers form near

the boundaries within a few ns after electrical breakdown. Quenching of excited species, recombination of ions and electrons, and gas heating are observed a few μs after the voltage pulse has ended. The effects of repetitive pulsing, such as accumulation of active species, become apparent over longer timescales (μs–ms). The numerical model should resolve both the sub-ns transients as well as slower processes taking place at ms timescales to provide useful information about the underlying physical phenomena. In addition, detailed chemistry mechanisms are essential for quantitative prediction of plasma heating rates and species production.

Recent intensified charge-coupled device (ICCD) images [20, 21] demonstrate that plane-to-plane pulsed NS DBDs in air appear uniform and diffuse, with plasma filling the entire gap volume at pressures in the range 40–100 Torr. Pre-heating has been shown to improve plasma uniformity and reduce filament formation in H_2–air and C_2H_4–air mixtures [20]. The presence of residual electrons and conductive heat loss to the walls are thought to play important roles in reducing temperature gradients and ionization instabilities in the discharge volume. Experimental measurements of O atom density using the two-atom laser-induced fluorescence (TALIF) technique and determination of temperature rise based on N_2 emission spectra [21] demonstrate that pulsed NS DBD can efficiently generate active radical species as well as gas heating. Quantitative information about other plasma generated chemical species and the nature of gas heating near the wall sheath layers, however, remains largely unknown.

The primary objective of this work is to establish a multi-scale theoretical/numerical framework to study the spatio-temporal evolution of nanosecond plasma over multiple discharge pulses with detailed chemical kinetics. Equations for electric potential, electron energy, and charged and neutral species continuity are considered. In addition, the conservation equations for mass, momentum and energy of the gas mixture are solved simultaneously to model flow motions. The electron transport and reaction coefficients are expressed as functions of electron energy from solutions of the Boltzmann equation [13]. An adaptive time-step approach is utilized to tackle the large disparity in timescales of various physical phenomena of interest. Implicit time integration is performed for stiff chemical source terms, whereas species and flow transport are treated explicitly for computational efficiency [22]. A domain decomposition approach with message passing interface (MPI) is implemented to compute the solution in parallel over multiple processors. This work complements and extends our previously reported modelling studies of nanosecond plasma [23, 24].

1D simulations of pulsed NS DBD in air are conducted in a plane-to-plane geometry in the pressure and pulsing frequency range 40–100 Torr and 1–10^5 Hz, respectively. The uniform and diffuse nature of the discharge in ICCD images [20, 21] justifies the 1D assumption. This work simulates the operating conditions and physical parameters such as voltage pulse shape and duration described in Yin *et al* [21]. The model predictions are validated against results of a quasi-1D analytical model [25] as well as experimental measurements [20, 21, 26, 27]. The underlying mechanisms and key chemical pathways governing plasma gas heating and radical species production are investigated in detail. Implications of current results on applications such as plasma-assisted ignition are discussed.

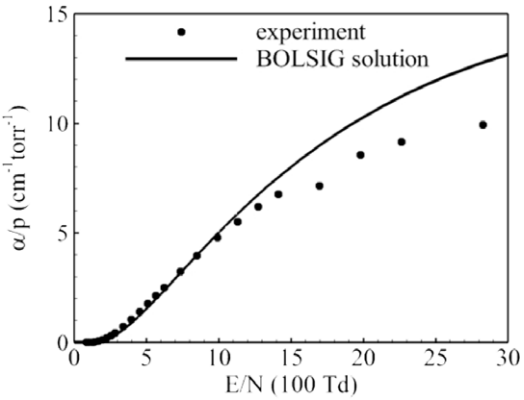

Figure 3. Comparison between Townsend ionization coefficients predicted by BOLSIG [13] and experiments [30] in nitrogen as a function of reduced electric field.

2. Theoretical framework

In this study, we use the plasma drift–diffusion fluid model with the 'local electron mean energy approximation' [28]. By adopting this strategy, the conservation of electron energy is enforced. The important assumptions and detailed derivation of the plasma fluid equations are provided in [29]. The electron transport and reaction-rate coefficients are expressed as functions of electron energy using BOLSIG [13], and updated at every time step through interpolation. The validity of this approach is verified in figure 3, which compares measurements of the Townsend ionization coefficient [30] in N_2 plasma with BOLSIG predictions as a function of E/N. The estimated ionization rate is in excellent agreement with measurements up to 1000 Td, and about 20% higher at 1500 Td. For the present NS DBD simulations, the reduced electric field is greater than 1000 Td only in the interior of the cathode sheath region (~0.2 mm thickness at 60 Torr and 300 K, see figure 6). The ionization rates in the cathode sheath, however, are negligible since it is essentially free of electrons. It has been shown that runaway ionization processes are dominant only in very short gaps and at low pressures even in extremely high electric fields [31, 32]. Hence, for conditions considered in this study, the electron-impact transport and reaction coefficients provided by BOLSIG are sufficiently accurate.

2.1. Governing equations

The continuity equation for each plasma species takes the following form,

$$\frac{\partial n_k}{\partial t} + \nabla \cdot \boldsymbol{J}_k = \dot{\omega}_k, \tag{1}$$

where n_k (cm^{-3}) is the number density of species k, and $\dot{\omega}_k$ (cm^{-3} s^{-1}) is the production term. The species flux

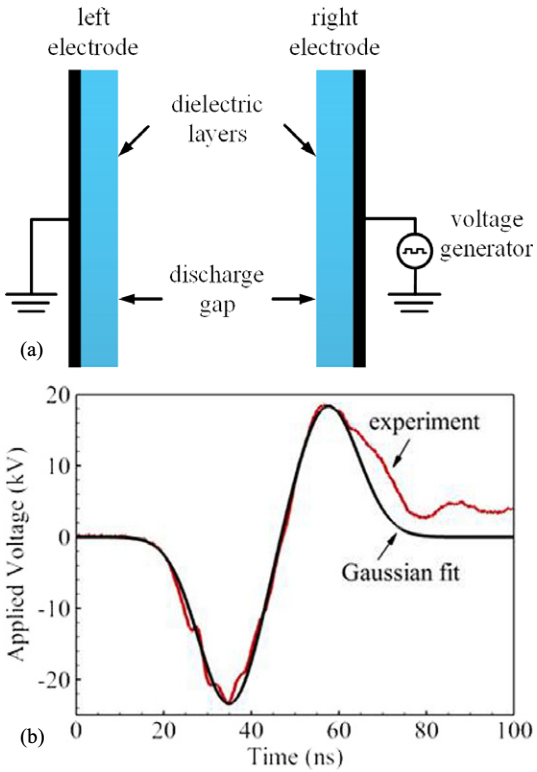

Figure 4. (*a*) Schematic of simulation configuration. (*b*) Gaussian fit to CPT experimental waveform [21] used in this work. The applied voltage shown is representative of a single discharge pulse. The same waveform is applied in a repetitive fashion at a prescribed frequency in the pulsed NS DBD simulations. The waveform shape was chosen to closely match the experimental waveform, which is not symmetrical.

$\boldsymbol{J}_k$ ($\mathrm{cm^{-2}\,s^{-1}}$) is obtained from the following equation:

$$\boldsymbol{J}_k = q_k \mu_k n_k \boldsymbol{E} - \boldsymbol{\nabla}(D_k n_k) + n_k \boldsymbol{u}, \tag{2}$$

where q_k is the charge number (-1 for negative ions and electrons, $+1$ for positive ions and 0 for neutral species), μ_k ($\mathrm{cm^2\,V^{-1}\,s^{-1}}$) the mobility in the electric field $\boldsymbol{E}$ ($\mathrm{V\,cm^{-1}}$), and D_k ($\mathrm{cm\,V^{-1}\,s^{-1}}$) the diffusion coefficient of species k. $\boldsymbol{u}$ ($\mathrm{cm\,s^{-1}}$) is the convection velocity of the gas mixture. The electron energy density n_ε ($\mathrm{eV\,cm^{-3}}$) is obtained from the following equation:

$$\frac{\partial n_\varepsilon}{\partial t} + \boldsymbol{\nabla}\cdot\boldsymbol{J}_\varepsilon = \dot{Q}_\varepsilon, \tag{3}$$

where n_ε is given by the product of electron number density,n_e, and the electron energy, ε. The flux J_ε ($\mathrm{eV\,cm^{-2}\,s^{-1}}$) and rate of production $\dot{Q}_\varepsilon$ ($\mathrm{eV\,cm^{-3}\,s^{-1}}$) are defined in equations (4) and (5).

$$\dot{Q}_\varepsilon = -\left(\frac{3k_\mathrm{B}m_\mathrm{e}}{eM}\right) n_\mathrm{e}\nu_\mathrm{el}(T_\mathrm{e} - T_\mathrm{g}) - \sum \Delta E_i r_i - \sum \boldsymbol{J}_e \cdot \boldsymbol{E} \tag{4}$$

$$\boldsymbol{J}_\varepsilon = -\mu_\varepsilon n_\varepsilon \boldsymbol{E} - \boldsymbol{\nabla}(D_\varepsilon n_\varepsilon) + n_\varepsilon \boldsymbol{u}, \tag{5}$$

where μ_ε ($\mathrm{cm^2\,V^{-1}\,s^{-1}}$) is the electron energy mobility, and D_ε ($\mathrm{cm\,V^{-1}\,s^{-1}}$) is the electron energy diffusion coefficient. The first term on the right-hand side of equation (5) denotes electron energy loss from elastic collisions with gas molecules, where n_e ($\mathrm{cm^{-3}}$) and υ_{el} ($\mathrm{s^{-1}}$) denote the number density and elastic collision frequency of electrons, respectively, m_e is the electron mass (kg), M is the average molecular mass of air (kg), T_e (K) is the electron temperature, and T_g (K) is the gas temperature. The second and third terms represent energy loss from electron-impact excitation and ionization reactions, and energy gain from acceleration in the applied field, respectively. ΔE_i (eV) is the heat of ith reaction with reaction rate r_i ($\mathrm{cm^{-3}\,s^{-1}}$) and $\boldsymbol{J}_\mathrm{e}$ the electron density flux ($\mathrm{cm^{-2}\,s^{-1}}$).

The electric potential φ (V) is computed using the Poisson equation below, with the electric field $\boldsymbol{E}$ obtained from equation (7),

$$\boldsymbol{\nabla}\cdot(\varepsilon\boldsymbol{\nabla}\varphi) = -e(n_+ - n_- - n_\mathrm{e}) \tag{6}$$

$$\boldsymbol{E} = -\boldsymbol{\nabla}\varphi, \tag{7}$$

where n_+ and n_- are the sum of number densities of positive ions and negative ions, respectively. The plasma fluid equations described previously are coupled with the following conservation equations of mass, momentum and energy.

$$\frac{\partial \rho}{\partial t} + \frac{\partial \rho u_i}{\partial x_i} = 0 \tag{8}$$

$$\frac{\partial \rho u_i}{\partial t} + \frac{\partial(\rho u_i u_j)}{\partial x_j} = -\frac{\partial p}{\partial x_i} + \frac{\partial \tau_{ij}}{\partial x_j} + F_i^\mathrm{EHD} \tag{9}$$

$$\frac{\partial \rho E}{\partial t} + \frac{\partial[(\rho E + p)u_i]}{\partial x_i} = -\frac{\partial q_i}{\partial x_i} + \frac{\partial(u_i\tau_{ij})}{\partial x_j} + \dot{Q}^\mathrm{JH}, \tag{10}$$

where ρ ($\mathrm{kg\,cm^{-3}}$) is the density of the plasma mixture, p ($\mathrm{kg\,cm^{-1}\,s^{-1}}$) is the pressure, and u_i and u_j are the flow velocity components in ith and jth directions, respectively. τ ($\mathrm{kg\,cm^{-1}\,s^{-2}}$) is the viscous shear stress tensor, q_j is the energy flux from heat conduction and diffusion, F_i^EHD is the electro-hydrodynamic force per unit volume, and $\dot{Q}^\mathrm{JH}$ is the heat release rate from Joule heating given by equations (11), (12), (13) and (14), respectively.

$$\tau_{ij} = \kappa(\partial u_i/\partial x_j + \partial u_j/\partial x_i) \tag{11}$$

$$q_j = -\lambda(\partial T/\partial x_j) + \rho\sum_k h_k Y_k D_k(\partial Y_k/\partial x_j) \tag{12}$$

$$F_i^\mathrm{EHD} = eE_i(n_+ - n_- - n_\mathrm{e}) \tag{13}$$

$$\dot{Q}^\mathrm{JH} = e\boldsymbol{E}\cdot\sum(\boldsymbol{J}_+ - \boldsymbol{J}_- - \boldsymbol{J}_\mathrm{e}), \tag{14}$$

where κ ($\mathrm{kg\,cm^{-1}\,s^{-1}}$) is the dynamic viscosity, λ ($\mathrm{W\,cm^{-1}\,K^{-1}}$) is the thermal conductivity of the gas mixture, and D_k is the effective diffusion coefficient for species k obtained using Wilke's mixing rule [33]. The total energy per unit volume ρE ($\mathrm{J\,cm^{-3}}$) is given by the following equation:

$$\rho E = \rho h - p + \rho(u_j u_j/2), \tag{15}$$

where h ($\mathrm{J\,kg^{-1}}$) is the mixture enthalpy per unit mass obtained from equation (16),

$$h = \sum_k Y_k\{h_k^0(T_\mathrm{ref}) + \int_{T_\mathrm{ref}}^{T} C_{p,k}(T')\,\mathrm{d}T'\}, \tag{16}$$

where h_k^0 and $C_{p,k}$ are the enthalpy of formation at a reference temperature T_ref, and the specific heat at constant pressure of species k, respectively.

2.2. Physical configuration

The physical configuration of concern is shown in figure 4(*a*). In all the cases considered in this study, the discharge geometry and operating conditions closely match the NS DBD flow reactor experiment in [21]. Two copper electrodes covered with a thin layer (1.75 mm thickness) of quartz as dielectric are placed 1 cm apart with the gap filled with synthetic air (79% N_2 and 21% O_2 by mole fraction) or pure N_2 (for comparison with analytical model results). A high-voltage pulse generator is connected to the right electrode in figure 4(*a*), whereas the left electrode is grounded at all times. The voltage pulse considered in this study is a Gaussian fit to the experimental CPT waveform [21] as shown in figure 4(*b*). The CPT pulse consists of a bipolar negative–positive waveform with voltage peaks at −22.5 kV and +20 kV, respectively. The total pulse duration is 100 ns with 12 ns FWHM each cycle.

2.3. Boundary conditions

At solid walls, a zero flux boundary condition is imposed for neutral species, with electron, positive ion and negative ion fluxes given by equations (17), (18) and (19), respectively [34],

$$\boldsymbol{J}_{e,s}\cdot\boldsymbol{n}_s=\frac{1}{4}n_e\left(\frac{8k_bT_e}{\pi m_e}\right)^{\frac{1}{2}}-a\sum_k\gamma\boldsymbol{J}_{+k,s}\cdot\boldsymbol{n}_s +(a-1)\mu_e n_e\boldsymbol{E}\cdot\boldsymbol{n}_s \tag{17}$$

$$\boldsymbol{J}_{+,s}\cdot\boldsymbol{n}_s=\frac{1}{4}n_+\left(\frac{8k_bT_g}{\pi m_+}\right)^{\frac{1}{2}}+a\mu_+n_+\boldsymbol{E}\cdot\boldsymbol{n}_s \tag{18}$$

$$\boldsymbol{J}_{-,s}\cdot\boldsymbol{n}_s=\frac{1}{4}n_-\left(\frac{8k_bT_g}{\pi m_-}\right)^{\frac{1}{2}}+(a-1)\mu_-n_-\boldsymbol{E}\cdot\boldsymbol{n}_s, \tag{19}$$

where $\boldsymbol{J}_{e,s}, \boldsymbol{J}_{+,s}, \boldsymbol{J}_{-,s}$ are the electron, positive ion and negative ion fluxes at the boundary, respectively, $\boldsymbol{n}_s$ is the normal vector pointing outwards, and γ (taken to be 0.05 [34]) the secondary electron emission coefficient for ionic species colliding with the surface. $a = 1$ if $\boldsymbol{E}\cdot\boldsymbol{n}_s < 0$, and $a = 0$ otherwise. The electron energy flux at the solid boundary is given by the following equation:

$$\boldsymbol{J}_{\varepsilon,s}\cdot\boldsymbol{n}_s=\left(\frac{5}{2}k_bT_e\right)\left[\frac{1}{4}n_e\left(\frac{8k_bT_e}{\pi m_e}\right)^{\frac{1}{2}}+(a-1)\mu_e n_e\boldsymbol{E}\cdot\boldsymbol{n}_s\right] -a\left(\frac{5}{2}k_bT_{se}\right)\sum_k\gamma\boldsymbol{J}_{+k,s}\cdot\boldsymbol{n}_s, \tag{20}$$

where $\boldsymbol{J}_{\varepsilon,s}$ is the electron energy flux at the wall, and T_{se} (assumed to be 1 eV [34]) is the temperature of secondary electrons ejected from the surface.

A zero flux condition is used for mass and momentum conservation equations at solid boundaries. Treatment of the wall boundary condition for the gas energy equation (equation (10)) needs special care. Rapid heating occurs in the cathode layer during each nanosecond voltage pulse, due to the ion Joule effect. Subsequent heat loss to the solid surface takes place over a much longer timescale. Because of the low thermal diffusivity of quartz ($\alpha \sim 1.4\times10^{-6}\,m^2\,s^{-1}$), only a small portion of the dielectric layer can be assumed to be affected by the heat transfer from the gas. We make use of analytic self-similar solutions for transient temperature distributions in a semi-infinite solid with constant heat flux [35] to arrive at the following expression for boundary temperature:

$$T_b=\frac{T_{amb}+G(t)^*T_{gw}}{1+G(t)};\qquad G(t)=\frac{4k_{gw}\sqrt{(\alpha_d t/\pi)}}{k_d\Delta x}, \tag{21}$$

where T_b, T_{amb}, and T_{gw} are the boundary temperature, external ambient temperature and gas temperature at a distance Δx from the wall, respectively. $G(t)$ is a non-dimensional heat transfer parameter, k_d is the thermal conductivity of quartz ($1.3\,W\,m^{-1}\,K^{-1}$), and k_{gw} is the thermal conductivity of the gas mixture ($W\,m^{-1}\,K^{-1}$) at temperature T_{gw}. $G(t)$ is negligibly small (less than 0.1) until about 2 ms, which indicates that the boundary is, in reality, closer to isothermal than adiabatic conditions.

The Poisson equation is solved only in the gas, assuming zero potential at the left boundary, and the gap voltage V_{gap} at right boundary. V_{gap} is obtained from the applied voltage V_{app} using the equation below [16]:

$$\frac{dV_{app}}{dt}=\left(1+\frac{2l_d}{\varepsilon_d L}\right)\frac{dV_{gap}}{dt}-\frac{2l_d e}{\varepsilon_d\varepsilon_0 L}\int_0^L[J_+-J_-]\,dx, \tag{22}$$

where L (cm) is the gap length, l_d (cm) is the thickness of the dielectric layer, ε_d is the dielectric constant (4.8 for quartz), and J_+ and J_- are the net positive and negative charge fluxes, respectively.

2.4. Numerical methods

A fractional time-step approach [22] is used to treat the convection–diffusion term and the chemical source term separately in the species equations. The spatial discretizations of species equations and conservation equations of mass, momentum and energy are performed using an exponential Scharfetter–Gummel scheme [36] and a MUSCL TVD scheme [37], respectively. Implicit time integration of electron continuity and energy equations is performed using a generalized minimal residual (GMRES)-based ODE solver [38]. The chemical source term in species equations is treated implicitly using a dense matrix solver [38]. The pre-processing of the plasma chemistry mechanism is carried out using subroutines available in an open-source zero-dimensional discharge solver, ZDPLASKIN [39]. Explicit time integration of species and flow conservation equations ion is performed with a fourth-order Runge–Kutta method. A uniform grid consisting of 1000 node points was found necessary to obtain a grid convergent solution. The solution is computed in parallel over multiple processors with domain decomposition using MPI. The strong coupling between electron density (solved in equation (1)) and electric potential (in equation (6)) results in a severe time-step restriction [40]. In order to overcome this constraint, the following semi-implicit form of the Poisson equation [40] is solved for electric potential,

$$\nabla\cdot\left(\varepsilon+\frac{e}{\varepsilon_0}\mu_e n_e\Delta t\right)\nabla\varphi=-\frac{e}{\varepsilon_0}(n_+-n_--n_e +\Delta t(\nabla.D_e\nabla n_e+S_e)). \tag{23}$$

Specifically, the electron density, n_e, at (k+1)th time step on the right-hand side of equation (6) is estimated by making use of the continuity equation for electrons (equation (1)). The above modifications to the Poisson equation have negligible effects on the accuracy of the results. An adaptive time-step approach [19] is adopted, taking advantage of the large disparity in the timescales of the dominant physical processes. The numerical time step is fixed at 1 ps during the voltage pulses. The electron energy equation and semi-implicit version of the Poisson equation are solved only during voltage pulses, since electric-field effects become negligible and the space charge density rapidly decays as the applied voltage goes to zero. Beyond this juncture, the electric field and space charge are set to zero, and the time step is raised to 1 ns. The time step is reset to 1 ps at the beginning of the next voltage pulse, and the process is repeated. By adopting this strategy, we are able to simulate a variety of physical phenomena occurring at different time scales (1 ps–10 ms) over multiple discharge pulses.

2.5. Plasma air chemistry

The chemical kinetic model of the air plasma used in this work consists of 20 species and 176 reactions. It is derived through a sensitivity study from a larger chemistry mechanism described in [26]. The model incorporates the neutral species N, N_2, O, O_2, O_3 and NO; charged species e^-, N_2^+, N_4^+, O_2^+, O_4^+ and O_2^-; and excited species $N_2(A\,^3\Sigma)$, $N_2(B\,^3\Pi)$, $N_2(C\,^3\Pi)$, $N_2(a'\,^1\Sigma)$, $O_2(a\,^1\Delta)$, $O_2(b\,^1\Sigma)$, $N(^2D)$ and $O(^1D)$. Atomic oxygen is the dominant species in air plasma generated by electron-impact dissociation of oxygen during voltage pulses and via excited nitrogen quenching by oxygen during afterglow. Other important neutral species include excited electronic states of nitrogen $A\,^3\Sigma$, $B\,^3\Pi$, $C\,^3\Pi$ and $a'\,^1\Sigma$, as well as ozone. The electron-impact reaction constants in $cm^{-3}\,s^{-1}$ units are expressed as functions of mean electron energy $\bar{\varepsilon}$, using BOLSIG, as discussed earlier. The uncertainty in electron-impact rate constants is about ±30%, and mainly depends on the accuracy of collision cross-section calculations and measurements [41]. For bi-molecular and tri-molecular reactions, the error limits depend inversely on the magnitude of rate constants [42], and can be as high as 100% for slower reactions. In addition, most of the rate measurements are performed at room temperature (300 K); this may be an additional source of error for temperature sensitive reactions. We have performed the simulations within the limitations of available kinetics data. Recent CARS measurements in air for plane–plane NS DBD [14] demonstrate that vibrational energy per molecule for the first ~100 pulses increases linearly with pulse number, and vibrational temperature levels off at ~1250 K. The vibrational relaxation takes 20–30 ms under present conditions [14]. Hence, vibrationally excited species are not explicitly included in the kinetic mechanism. The energy coupled to the plasma when E/N is below 100 Td is assumed to be 'locked' in the N_2 molecules and not considered as a source of gas heating.

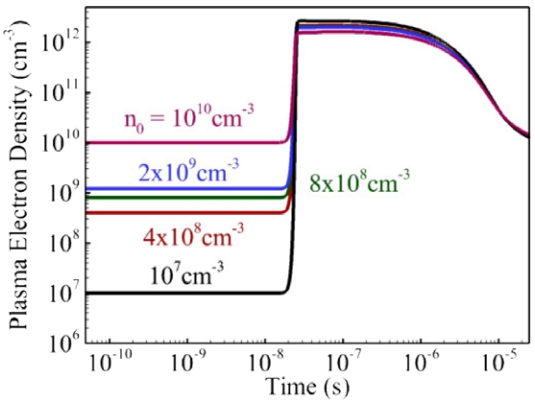

Figure 5. Sensitivity of evolution of electron number density in plasma ($x = 0.5$ cm location) for changes in initial electron density.

3. Results and discussion

In this section, we describe the physiochemical nature of pulsed NS DBD with the help of 1D simulations, which are validated against experimental data and analytical model calculations. All simulations are performed assuming a constant initial electron density in the computational domain. Due to the repetitive nature of the discharge process, the residual electrons from one pulse are responsible for initiation of discharge during subsequent pulses. Figure 5 shows that the nanosecond discharge is weakly sensitive to variation in initial electron densities. The electron number density in the quasi-neutral plasma ($x = 0.5$ cm) after breakdown differs by about 10% when the initial electron density is increased by one order of magnitude. In the presence of residual electrons, photo-ionization does not play an important role in initiating the discharge, and hence is not considered as a source term in the electron and positive ion continuity equations.

3.1. Comparison with analytical model

Adamovich *et al* [25] developed a quasi-1D model to describe the energy coupling in the plasma based on experimental evidence of uniformity of NS DBD. The model demonstrates that the input energy is primarily a function of breakdown voltage and capacitance of dielectric layers, as given by the following relation:

$$Q_{\text{pulse}} \approx \frac{1}{2}C\left[V_b^2 + V_{\text{peak}}^2\frac{\sqrt{2\pi}}{(\tau/RC)}\right] = \frac{1}{2}\frac{\varepsilon_d\varepsilon_0 A}{2l_d}\left[V_b^2 + V_{\text{peak}}^2\frac{\sqrt{2\pi}}{(\tau/RC)}\right], \quad (24)$$

where Q_{pulse} is the input pulse energy, C is the effective capacitance of dielectric layers on electrodes, V_b and V_{peak} breakdown voltage and peak voltage, respectively, R is the resistance of shielded plasma after breakdown, τ is the pulse duration parameter in Gaussian fit of voltage waveform, ε_d and l_d are the dielectric constant and dielectric thickness, respectively, and A is the electrode surface area. Similar analytic expressions have been obtained for electric field and electron density in the plasma, cathode sheath location and

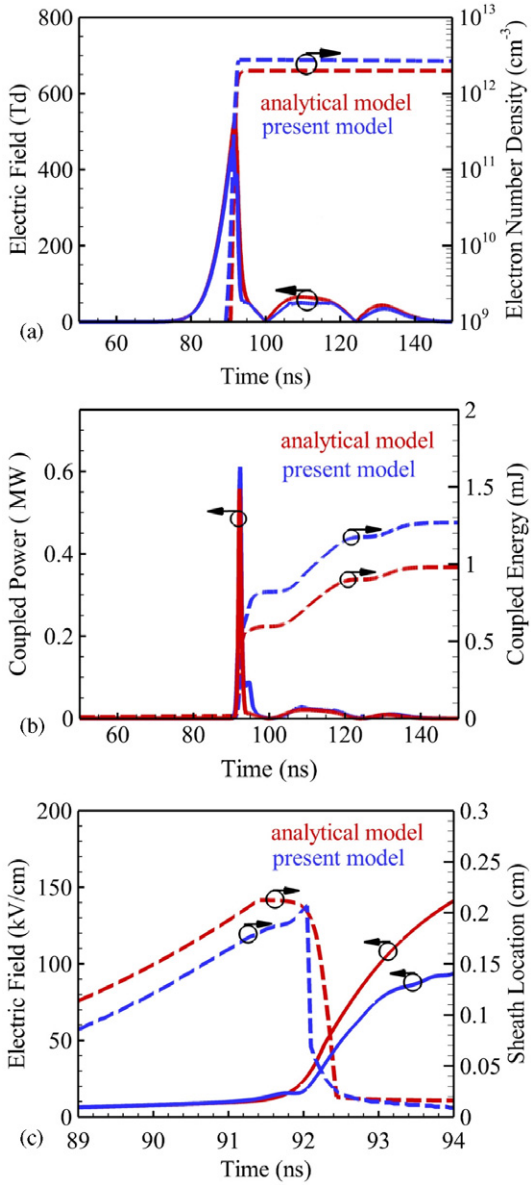

Figure 6. Comparison between analytical model results [25] and 1D model predictions for nanosecond discharge in N_2 at 60 Torr and 300 K. (*a*) Electric field and electron number density in quasi-neutral plasma ($x = 0.5$ cm for 1D model), (*b*) input electrical power and input energy to the discharge, and (*c*) location of cathode sheath and electric field at sheath boundary as functions of time.

electric field at the sheath edge, and input power during the voltage pulse.

Figure 6 shows a comparison between analytical results and the present 1D model calculations. The simulation is performed in pure N_2 at 300 K and 60 Torr initial temperature and pressure, respectively, using only nitrogen-based species from the plasma air chemistry mechanism described in section 2.5. The voltage waveform is a positive–negative bipolar pulse with voltage peaks at 23.5 kV and −17.5 kV, respectively, FWHM 10 ns for each cycle, and pulse duration of 200 ns. Good agreement with analytical calculations provides confidence in the 1D model predictions. It is evident in figure 6(*a*) that peak electric field in the plasma is approximately 500 Td. After breakdown, the electric field in the plasma drops rapidly due to positive and negative space charge accumulation at the cathode and anode sheath boundaries. The coupled power and energy shown in figure 6(*b*) are calculated using the following relations for the present model:

$$W_\mathrm{p} = A\left|\int_0^L e\boldsymbol{E}\cdot(\boldsymbol{J}_+ - \boldsymbol{J}_- - \boldsymbol{J}_e)\,\mathrm{d}x\right|;$$

$$Q_\mathrm{p} = \int_0^{T_\mathrm{p}} W_\mathrm{p}\,\mathrm{d}t, \tag{25}$$

where W_p and Q_p are the coupled power (W) and coupled energy (J), respectively, and T_p is the pulse duration. Approximately 60% of the pulse energy is input during the breakdown process. The remaining energy is coupled when the field in the plasma reverses in direction. Similar behaviour is observed for discharges in air as described in the next section. Figure 6(*c*) depicts the location of the cathode sheath boundary and electric field at that location during breakdown. The quasi-steady sheath is located at ∼0.2 mm, as predicted by the model. The electric field in the sheath reaches 140 kV cm^{-1} when the sheath attains its quasi-steady location. The deviations in the sheath field predicted by the present 1D analysis and the analytical model can be attributed to differences in electron-impact ionization rates obtained from BOLSIG and experimental curve fits employed in the analytical model.

3.2. Repetitively pulsed NS DBD in air

The plasma chemistry mechanism described in section 2.5 is utilized for simulations of plasma discharge in air. Figure 7 shows the temporal evolution of the electric field and electron energy in the computational domain. The simulation was performed at an initial pressure and temperature of 62 Torr and 300 K, respectively. The Gaussian fit of the CPT waveform shown in figure 4(*b*) is employed, with the voltage pulses applied at 40 kHz repetition rate. The initial electron density is fixed at 4×10^8 cm^{-3}. The reduced electric field (E/N) at the centre of the discharge volume ($x = 0.5$ cm) is shown in figure 7(*a*). The peak value of E/N (∼450 Td) occurs during the primary breakdown stage approximately 25 ns from the beginning of the voltage pulse. Positive and negative space charge accumulation at the cathode and anode sheath boundaries, respectively, causes the gap voltage to drop and the field in the plasma rapidly falls to zero (by 28 ns). Two subsequent, albeit smaller, peaks in E/N are observed at around 38 and 60 ns; the time derivative of the applied voltage changes sign, causing the electric field in the plasma to change its direction. The additional energy coupled to the plasma goes almost exclusively to the vibrational mode, since E/N remains less than 60 Td during the two secondary breakdown phases. Repeated application of voltage pulses results in a periodic behaviour of the discharge process, with the peak of E/N remaining nearly constant from pulse to pulse; the energy input during each voltage pulse remains fairly constant until a noticeable rise in temperature occurs.

The initiation of the nanosecond discharge can be clearly seen in figure 7(*b*), which depicts the spatial variation in the electric field. At 25 ns, an ionization wave moves rapidly

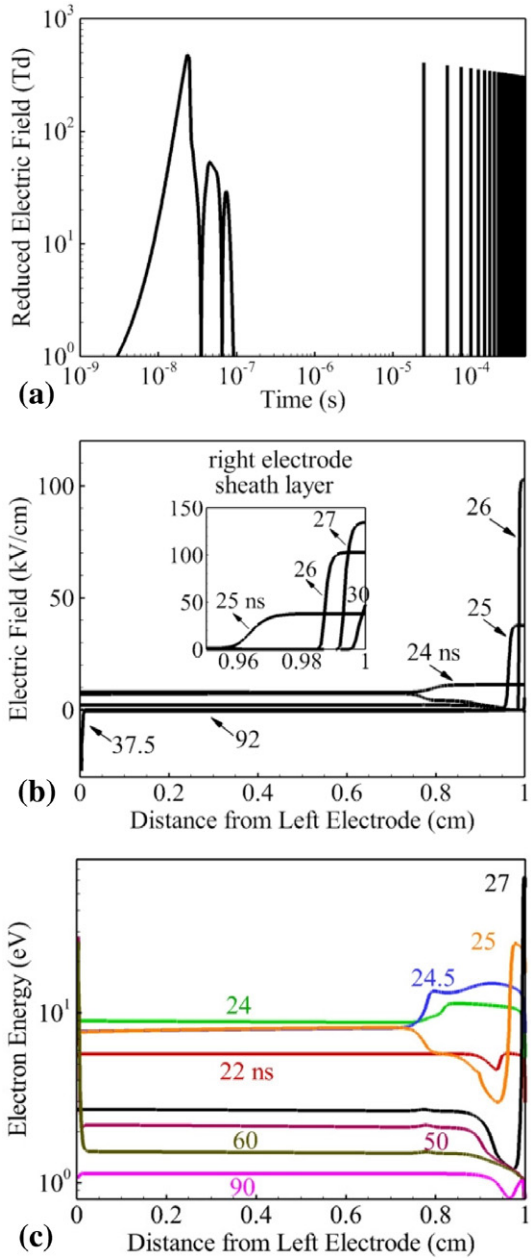

Figure 7. (*a*) Temporal evolution of reduced electric field for 25 voltage pulses. Spatial variation in (*b*) electric field, and (*c*) electron energy during the first voltage pulse. Simulation conducted in air at 60 Torr and 300 K initial pressure and temperature, respectively, at 40 kHz repetition rate.

towards the right electrode (which serves as the cathode for the negative half cycle of the CPT pulse), resulting in uniform production of charged and excited species in the discharge volume. A narrow sheath region develops near the cathode of ∼0.2 mm thickness at 27 ns, with the electric field reaching 140 kV cm^{-1}. It must be noted that the two-term expansion of the electron Boltzmann equation over-predicts ionization rates in high electric fields (shown in figure 3). Owing to the low electron density near the cathode and a small sheath thickness; however, the error incurred in predicting the overall discharge dynamics is not significant.

The evolution of electron energy during the discharge pulse is shown in figure 7(*c*). The overall trend follows that

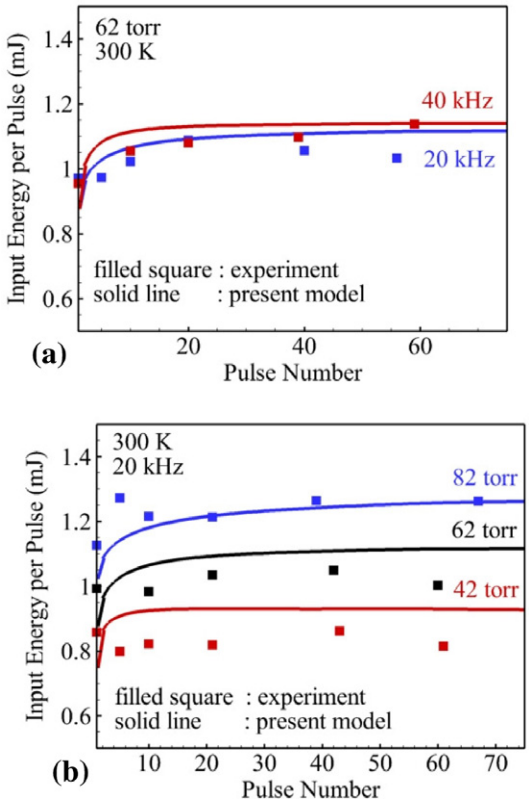

Figure 8. Comparison of input energy predictions with experimental measurements from [21], at (*a*) 62 Torr and 300 K initial pressure and temperature, respectively, and (*b*) 300 K initial temperature and 20 kHz pulsing rate.

of the electric field with a peak value of 9 eV in the plasma volume at 25 ns when breakdown occurs. The electron energy in the region near the right electrode continues to rise and reaches 75 eV when the cathode sheath reaches its quasi-steady location. The left electrode serves as a cathode in the positive half cycle of the CPT pulse, with electron energy peaking at 40 eV, close to the left boundary, at 60 ns.

Yin *et al* [21] reported coupled pulse energy measurements during NS DBD at various pressures and repetition rates. Figure 8 shows the model predictions using the expression in equation (25) validated against experimental data. The input energy per pulse is a weak function of repetition frequency, as evident in figure 8(*a*). The operating conditions are 62 Torr and 300 K for the initial pressure and temperature, respectively, using CPT waveforms to initiate the discharge. The model predictions are within 20% of the measured input energy of ∼1.1 mJ per pulse, and remain fairly constant with pulse number. Figure 8(*b*) indicates that the coupled energy increases linearly with pressure, in line with experimental observations. In general, the input energy has been shown [21] to vary linearly with the number density and drop at higher pulse numbers (beyond ∼200 pulses for a repetition rate of 40 kHz), due to a noticeable increase in temperature from the plasma heating process.

Figure 9 shows the production and decay of charged species during and after a high-voltage pulse. During the primary breakdown phase (24–26 ns), a fast ionization wave propagates rapidly towards the cathode (right electrode,

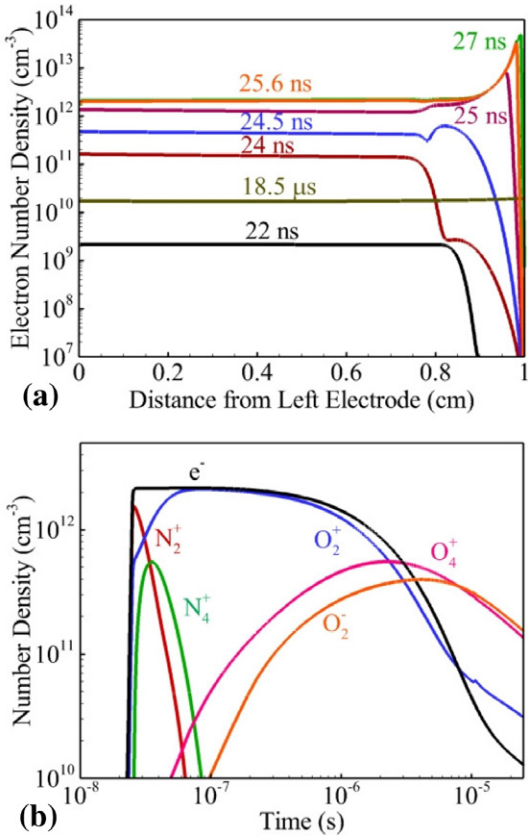

Figure 9. (*a*) Spatial and temporal evolution of electron density during a voltage pulse. (*b*) Variation of charged species densities in quasi-neutral plasma ($x = 0.5$ cm) as a function of time after a single nanosecond voltage pulse. Discharge in air at 60 Torr initial pressure and 300 K initial temperature.

resulting in fairly uniform production of electrons over the entire domain, as evident in figure 9(*a*). The peak is located near the sheath boundary ∼0.3 mm from the right electrode, with the electron density an order of magnitude greater than that in the rest of the discharge volume (5×10^{13} cm^{-3} versus 2×10^{12} cm^{-3}). The disparity in time scales of production and decay of charged species in the plasma afterglow can be seen in figure 9(*b*). N_2^+ and O_2^+ are the dominant positive ions produced via electron-impact ionization reactions during the primary breakdown timescale. By the end of the voltage pulse, N_2^+ is almost completely transformed to N_4^+ via three-body reaction and to O_2^+ via charge exchange reaction, given in (R1) and (R2) [42], respectively.

$$N_2^+ + N_2 + M \rightarrow N_4^+ + M \quad \text{(R1)}$$

$$N_2^+ + O_2 \rightarrow O_2^+ + N_2. \quad \text{(R2)}$$

Decay of electron density occurs primarily through dissociative recombination of O_2^+ and N_2^+ and attachment reactions with O_2 forming O_2^- given by (R3) and (R4), respectively [42]. O_4^+ and O_2^- are the dominant charged species present in air plasma after 20 μs, by which time the electron density drops to $\sim 10^{10}$ cm^{-3} in the entire domain.

$$O_2^+(N_2^+) + e \rightarrow O(N) + O(N) \quad \text{(R3)}$$

$$e + O_2 + O_2 \rightarrow O_2^- + O_2 \quad \text{(R4)}$$

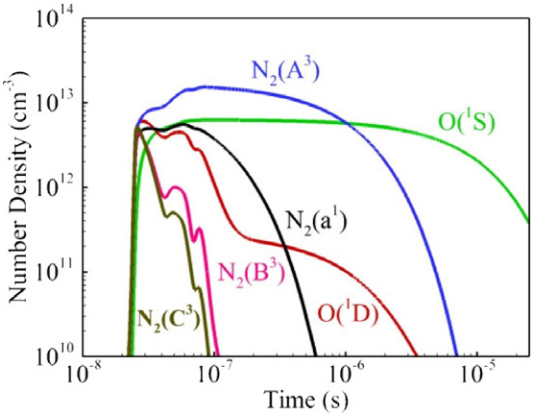

Figure 10. Time evolution of short lived electronically excited species after a single nanosecond pulse in air at 60 Torr and 300 K initial pressure and temperature, respectively.

Electronically excited N_2 species are produced with high efficiency in NS DBD during the initial breakdown phase, as seen in figure 10. This phenomenon can be attributed to E/N in the range 100–300 Td, when electronic excitation is the dominant electron-impact processes [43]. Quenching of these excited species by O_2 is an important pathway for production of ground state and excited oxygen atoms, given in the following equation [44, 45].

$$N_2(A^3, B^3, C^3, a^1) + O_2 \rightarrow N_2 + O + O\,(O(^1D), O(^1S)). \quad \text{(R5)}$$

Longer lifetime active species such as O and $O_2(a^1)$ produced by nanosecond discharges have been shown to significantly influence ignition and combustion processes in fuel and air mixtures [1]. Figure 11(*a*) shows the TALIF O atom measurements after a single nanosecond pulse [26], and for a 100 pulse burst [27], compared with model predictions in quasi-neutral plasma ($x = 0.5$ cm). Good agreement for both single pulse and burst mode (100 kHz) cases suggest that the current kinetic model adequately describes the important O atom production and destruction pathways. Temporal evolution of important long time active species in the quasi-neutral plasma region for NS DBD in air (40 kHz repetition rate) is depicted in figure 11(*b*). Atomic oxygen is primarily produced via electron-impact dissociation during the discharge pulses (R6), and then from quenching of electronically excited N_2 species by O_2 (R5), evident in figure 11(*c*). Approximately 40% of the O production occurs via (R6), a majority of which happens within the primary breakdown phase (25–28 ns) of the voltage pulse. The remaining 60% is produced over ∼200 ns, by which time the electronically excited N_2 species are completely quenched. Formation of ozone via three-body reaction (R7) is the primary destruction pathway for O atom. This is a slow process and can equal or exceed O production rates only in the ms timescale.

$$O_2 + e \rightarrow O + O(O(^1D), O(^1S)) + e \quad \text{(R6)}$$

$$O + O_2 + M \rightarrow O_3 + M. \quad \text{(R7)}$$

Singlet delta oxygen, $O_2(a^1)$, is produced via electron-impact excitation reactions during the discharge pulse, and later

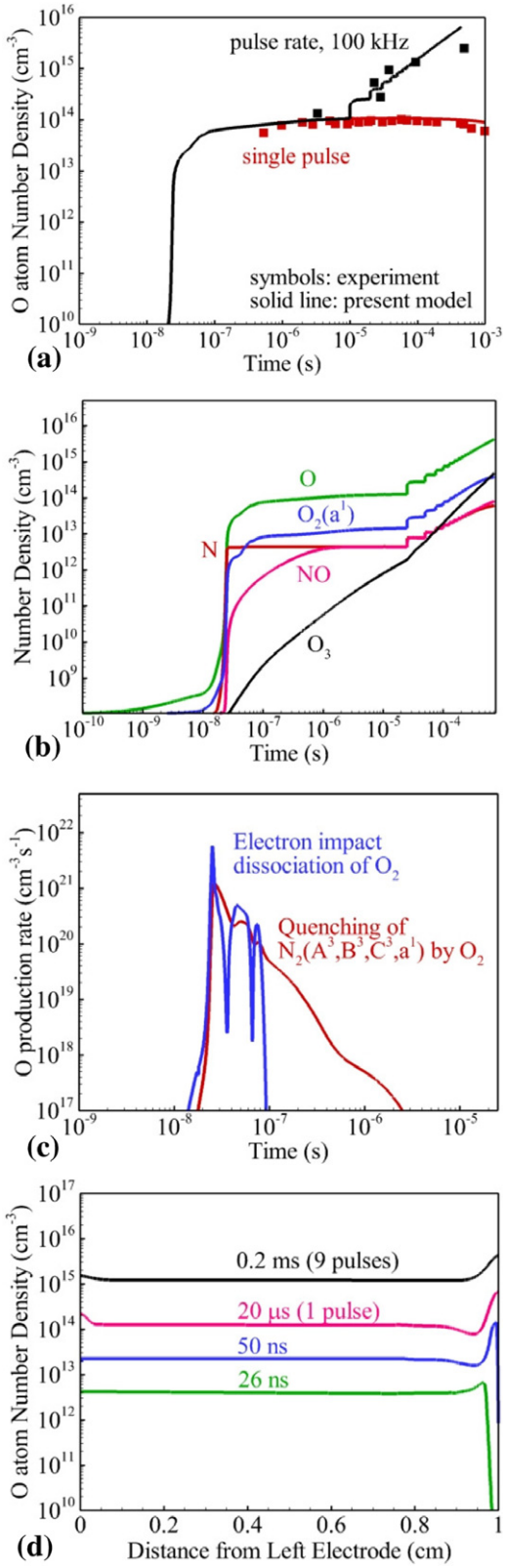

Figure 11. (*a*) TALIF O atom measurements after a single nanosecond pulse [26], and for a 100 pulse burst (100 kHz repetition rate) [27] compared with model predictions. (*b*) Temporal evolution of long lifetime active species in quasi-neutral plasma ($x = 0.5$ cm). (*c*) O production rate via electron-impact dissociation and quenching of excited N_2 species by O_2 during and after first voltage pulse. (*d*) Spatial evolution of O density at various times. All simulations performed at 60 Torr initial pressure and 300 K temperature, and 40 kHz repetition rate for cases depicted in (*b*), (*c*) and (*d*).

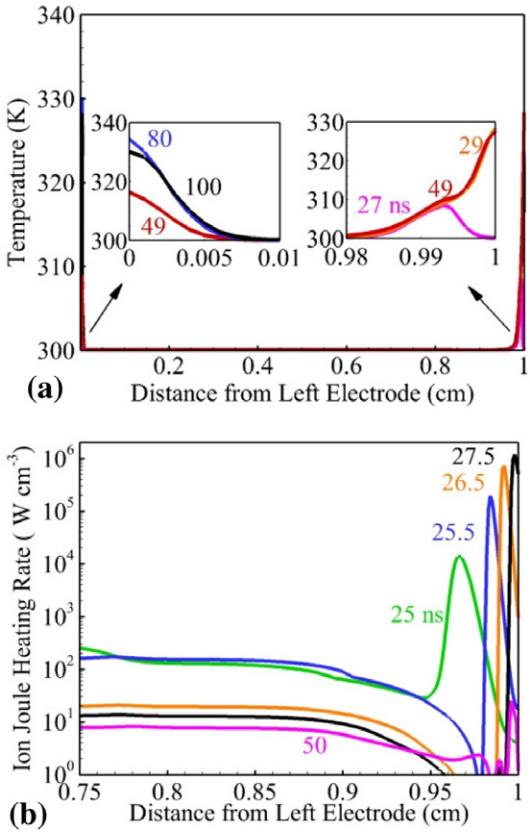

Figure 12. Spatial variation in (*a*) temperature, and (*b*) ion Joule heating rate during a single discharge pulse at 60 Torr and 300 K initial pressure and temperature.

through relaxation of $O_2(b^1)$ excited state. Note that under the present conditions, $O_2(a^1)$ densities are an order of magnitude smaller than O atom densities, and the latter is clearly the dominant active species produced by pulsed NS DBD in air. Figure 11(*d*) shows the spatial distribution of atomic oxygen from ns-ms timescales. The profiles are fairly uniform over the entire domain with a peak near the right electrode, where electron and excited N_2 densities are relatively high during the discharge pulses (see figure 9(*a*)). The destruction rate (R7) exceeds the production rate by 2 ms, especially near the peaks, resulting in more uniform spatial profiles.

In addition to producing active species, nanosecond plasma discharges may also influence ignition and combustion processes by heating the gas mixture over both short (ns) and long (μs–ms) timescales. During a high-voltage pulse, rapid heating is observed only near the boundaries, as shown in figure 12(*a*). Temperatures at the extremities rise by approximately 40 K within 100 ns. Ion Joule heating arising from the high electric fields in the sheath during breakdown, shown in figure 12(*b*), is responsible for this fast temperature rise. Note that both plots are shown over the duration of the first discharge pulse, with an initial temperature of 300 K over the entire domain.

In figure 13, the experimental measurements of temperature are plotted against model predictions at the centre of the discharge volume over multiple discharge pulses at 40 kHz repetition rate with CPT waveform. The model results

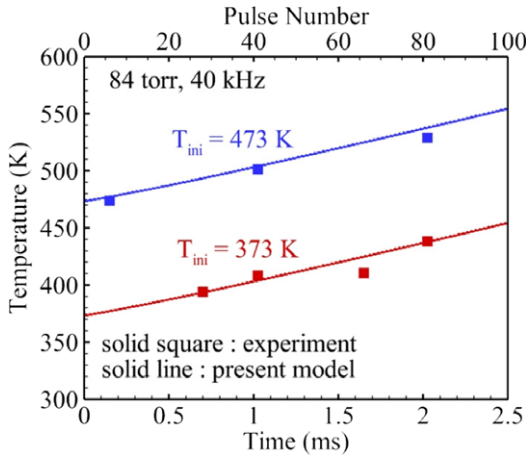

Figure 13. Comparison of measurements [20] and model predictions of temperature as a function of time at the centre of the discharge volume at 84 Torr initial pressure, 40 kHz repetition rate, and initial temperatures of 373 K and 473 K.

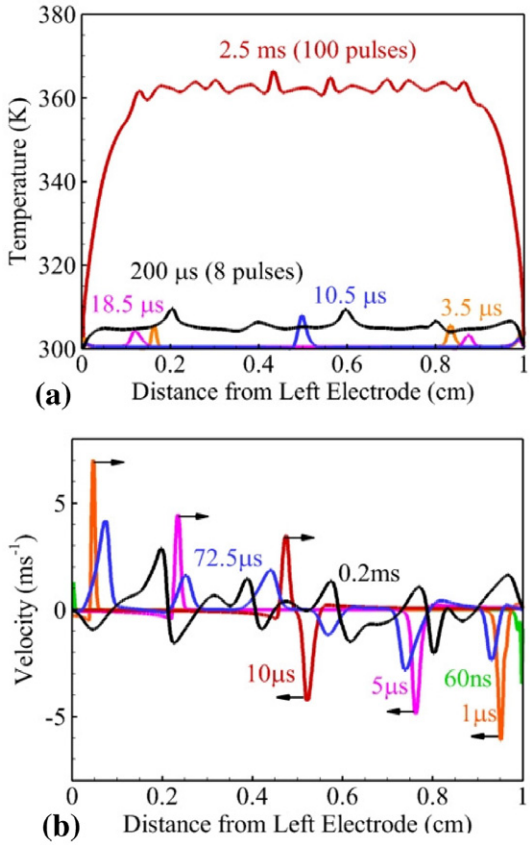

Figure 14. Spatial variation of (*a*) temperature, and (*b*) bulk velocity over multiple discharge pulses for 60 Torr initial pressure and 300 K initial temperature at 40 kHz repetition rate.

are in line with measured values, suggesting that temperature rise in air subjected to NS DBD is ∼0.5–1 K/pulse. Heating rates in fuel–air mixtures have been observed to be much greater, mainly due to higher chemical heat release from partial fuel oxidation [20].

Chemical heat release from electron–ion recombination and quenching of excited species causes a fairly uniform temperature rise with kinks arising from waves generated from ion Joule heating, as shown in figure 14(*a*). The diffusive heat loss to the cooler sections of the gas, along with conduction at the wall, results in rapid dissipation of thermal energy arising from ion Joule heating. It must be emphasized that intense heating rates are present only for a few ns during the breakdown process. The loss mechanisms, on the other hand, occur over several μs, and prevent overheating of the cathode layer and development of ionization instabilities. An interesting consequence of rapid ion Joule heating is formation of weak acoustic waves, which propagate into the discharge volume from both electrodes, as shown in figure 14(*b*). The speed of these acoustic waves can be estimated as ∼500 ms^{-1}, which at 300 K in air is equivalent to a Mach 1.42 shock wave. Note that a normal adiabatic shock at this Mach number would result in a temperature rise of approximately 78 K. Homogeneous distribution of active species and thermal energy by pulsed NS DBD may help explain the volumetric ignition observed in preheated H_2–air and mixtures recently reported in [20], as opposed to traditional ignition at a hotspot.

4. Conclusion

A comprehensive analysis is performed to study the dynamics of energy coupling, gas heating, and generation of active species by repetitively pulsed nanosecond dielectric barrier discharges (NS DBDs) in air. The simulations were performed with pressures between 40 and 100 Torr, and pulsing frequency in the range 1–10^5 Hz. Results show good agreement with measurements of coupled energy, O atom density and temperature in the discharge. During each high-voltage pulse, the discharge develops in the form of a fast ionization wave resulting in nearly uniform excitation and dissociation of the gas mixture via electron-impact reactions. The input electrical energy is directly proportional to the number density, and remains fairly constant on a per molecule basis from pulse to pulse. Repetitive pulsing causes uniform production of atomic oxygen in the discharge volume via electron-impact dissociation during voltage pulses, and through quenching of excited nitrogen molecules in the afterglow. Charge accumulation at the sheath boundary causes the field in the plasma volume to drop immediately after breakdown. The field in the cathode sheath (∼0.2 mm thickness), however, continues to rise with applied voltage, resulting in rapid gas heating through ion Joule effect, of approximately 40 K within 50 ns. Diffusion in the gas and conductive heat loss to the walls between voltage pulses prevents overheating of the cathode layer and development of ionization instabilities. A uniform temperature profile developed in the discharge volume after multiple pulses (∼100 pulses) as a consequence of the chemical heat release from quenching of excited species. This finding explains recent experimental observations of volumetric ignition (as opposed to hot-spot ignition) in fuel–air mixtures subject to NS DBD.

Acknowledgments

This work was supported by an MURI research grant FA9550-09-0602 from the Air Force Office of Scientific Research, with Dr Chiping Li as technical monitor.

References

[1] Starikovskiy A and Aleksandrov N 2013 Plasma-assisted ignition and combustion *Science* **39** 61–110

[2] Starikovskaia S 2006 Plasma assisted ignition and combustion *J. Phys. D: Appl. Phys.* **39** R265

[3] Starikovskii A Y 2005 Plasma supported combustion *Proc. Combust. Inst.* **30** 2405–17

[4] Leonov S B, Yarantsev D A, Napartovich A P and Kochetov I V 2006 Plasma-assisted combustion of gaseous fuel in supersonic duct *IEEE Trans. Plasma Sci.* **34** 2514–25

[5] Dutta A, Yin Z and Adamovich I V 2011 Cavity ignition and flameholding of ethylene–air and hydrogen–air flows by a repetitively pulsed nanosecond discharge *Combust. Flame* **158** 1564–76

[6] Kim W, Do H, Mungal M G and Cappelli M A 2006 Plasma-discharge stabilization of jet diffusion flames *IEEE Trans. Plasma Sci.* **34** 2545–51

[7] Pilla G, Galley D, Lacoste D A, Lacas F, Veynante D and Laux C O 2006 Stabilization of a turbulent premixed flame using a nanosecond repetitively pulsed plasma *IEEE Trans. Plasma Sci.* **34** 2471–7

[8] Adamovich I V, Lempert W R, Nishihara M, Rich J W and Utkin Y G 2008 Repetitively pulsed nonequilibrium plasmas for magnetohydrodynamic flow control and plasma-assisted combustion *J. Propul. Power* **24** 1198

[9] Adamovich I, Choi I, Jiang N, Kim J, Keshav S, Lempert W, Mintusov E, Nishihara M, Samimy M and Uddi M 2009 Plasma assisted ignition and high-speed flow control: non-thermal and thermal effects *Plasma Sources Sci. Technol.* **18** 034018

[10] Laroussi M, Hynes W, Akan T, Lu X and Tendero C 2008 The plasma pencil: a source of hypersonic cold plasma bullets for biomedical applications *IEEE Trans. Plasma Sci.* **36** 1298–9

[11] Shi J, Zhong F, Zhang J, Liu D and Kong M G 2008 A hypersonic plasma bullet train traveling in an atmospheric dielectric-barrier discharge jet *Phys. Plasmas* **15** 013504

[12] Ayan H, Staack D, Fridman G, Gutsol A, Mukhin Y, Starikovskii A, Fridman A and Friedman G 2009 Application of nanosecond-pulsed dielectric barrier discharge for biomedical treatment of topographically non-uniform surfaces *J. Phys. D: Appl. Phys.* **42** 125202

[13] Hagelaar G and Pitchford L 2005 Solving the Boltzmann equation to obtain electron transport coefficients and rate coefficients for fluid models *Plasma Sources Sci. Technol.* **14** 722

[14] Montello A, Yin Z, Burnette D, Adamovich I and Lempert W 2012 Picosecond CARS measurements of nitrogen vibrational loading and rotational/translational temperature in non-equilibrium discharges *50th AIAA Aerospace Sciences Meeting (Nashville, TN)*

[15] Uddi M, Jiang N, Frederickson K, Mintoussov E, Adamovich I V and Lempert W R 2007 Oxygen atom measurements in a nanosecond pulse discharge by two photon absorption laser induced fluorescence *38th AIAA Plasmadynamics and Lasers Conf. (Miami, FL)*

[16] Macheret S O, Shneider M N and Miles R B 2002 Modeling of air plasma generation by repetitive high-voltage nanosecond pulses *IEEE Trans. Plasma Sci.* **30** 1301–14

[17] Pancheshnyi S, Nudnova M and Starikovskii A 2005 Development of a cathode-directed streamer discharge in air at different pressures: experiment and comparison with direct numerical simulation *Phys. Rev.* E **71** 016407

[18] Unfer T and Boeuf J P 2009 Modelling of a nanosecond surface discharge actuator *J. Phys. D: Appl. Phys.* **42** 194017

[19] Poggie J, Adamovich I V, Bisek N and Nishihara M 2013 Numerical simulation of nanosecond pulse electrical discharges *Plasma Sources Sci. Technol.* **22** 015001

[20] Yin Z, Takashima K and Adamovich I V 2011 Ignition time measurements in repetitive nanosecond pulse hydrogen–air plasmas at elevated initial temperatures *IEEE Trans. Plasma Sci.* **39** 3269–82

[21] Yin Z, Takashima K and Adamovich I V 2013 Measurements and kinetic modeling of energy coupling in volume and surface nanosecond pulse discharges *Plasma Sources Sci. Technol.* **22** 015013

[22] Hsieh S Y and Vigor Y 1997 A preconditioned flux-differencing scheme for chemically reacting flows at all Mach numbers *Int. J. Comput. Fluid Dyn.* **8** 31–49

[23] Nagaraja S and Yang V 2012 chemical and transport effects of nanosecond discharges in H_2–air and C_2H_4–air mixtures *50th AIAA Aerospace Sciences Meeting (Nashville, TN)*

[24] Nagaraja S and Yang V 2011 nanosecond plasma enhanced counterflow diffusion flames *42nd AIAA Plasmadynamics and Lasers Conf. (Honululu, Hawaii)*

[25] Adamovich I V, Nishihara M, Choi I, Uddi M and Lempert W R 2009 Energy coupling to the plasma in repetitive nanosecond pulse discharges *Phys. Plasmas* **16** 113505

[26] Uddi M, Jiang N, Mintusov E, Adamovich I V and Lempert W R 2009 Atomic oxygen measurements in air and air/fuel nanosecond pulse discharges by two photon laser induced fluorescence *Proc. Combust. Inst.* **32** 929–36

[27] Zuzeek Y, Choi I, Uddi M, Adamovich I V and Lempert W R 2010 Pure rotational CARS thermometry studies of low-temperature oxidation kinetics in air and ethene–air nanosecond pulse discharge plasmas *J. Phys. D: Appl. Phys.* **43** 124001

[28] Davoudabadi M, Shrimpton J and Mashayek F 2009 On accuracy and performance of high-order finite volume methods in local mean energy model of non-thermal plasmas *J. Comput. Phys.* **228** 2468–79

[29] Gogolides E and Sawin H H 1992 Continuum modeling of radio-frequency glow discharges: I. Theory and results for electropositive and electronegative gases *J. Appl. Phys.* **72** 3971–87

[30] Haydon S and Williams O 2001 Combined spatial and temporal studies of ionization growth in nitrogen *J. Phys. D: Appl. Phys.* **9** 523

[31] Tarasenko V F and Yakovlenko S I 2007 The electron runaway mechanism in dense gases and the production of high-power subnanosecond electron beams *Phys.—Usp.* **47** 887

[32] Tkachev A N and Yakovlenko S I 2004 Runaway of electrons in dense gases and mechanism of generation of high-power subnanosecond beams *Cent. Eur. J. Phys.* **2** 579–635

[33] Wilke C 1950 A viscosity equation for gas mixtures *J. Chem. Phys.* **18** 517–9

[34] Wang Q, Economou D J and Donnelly V M 2006 Simulation of a direct current microplasma discharge in helium at atmospheric pressure *J. Appl. Phys.* **100** 023301

[35] Incropera F D, Bergman D and Lavine T A 2007 *Fundamentals of Heat and Mass Transfer* (New York: Wiley)

[36] Kulikovsky A 1999 Two-dimensional simulation of the positive streamer in N_2 between parallel-plate electrodes *J. Phys. D: Appl. Phys.* **28** 2483

[37] Hindmarsh A C, Brown P N, Grant K E, Lee S L, Serban R, Shumaker D E and Woodward C S 2005 SUNDIALS: suite of nonlinear and differential/algebraic equation solvers *ACM Trans. Math. Softw. (TOMS)* **31** 363–96

[38] Kurganov A and Tadmor E 2000 New high-resolution central schemes for nonlinear conservation laws and convection–diffusion equations *J. Comput. Phys.* **160** 241–82

[39] Pancheshnyi S, Eismann B, Hagelaar G and Pitchford L 2008 ZDPlasKin: a new tool for plasmachemical simulations *61st Annual Gaseous Electronics Conf. (Dallas, TX)*

[40] Arslanbekov R R and Kolobov V I 2003 Two-dimensional simulations of the transition from Townsend to glow discharge and subnormal oscillations *J. Phys. D: Appl. Phys.* **36** 2986

[41] Itikawa Y 2006 Cross sections for electron collisions with nitrogen molecules *J. Phys. Chem. Ref. Data* **35** 31–54

[42] Sieck L W, Heron J T and Green D S 2000 Chemical kinetics database and predictive schemes for humid air plasma chemistry: I. Positive ion–molecule reactions *Plasma Chem. Plasma Process.* **20** 235–58

[43] Popov N 2011 Fast gas heating in a nitrogen–oxygen discharge plasma: I. Kinetic mechanism *J. Phys. D: Appl. Phys.* **44** 285201

[44] Aleksandrov N, Anokhin E, Kindysheva S, Kirpichnikov A, Kosarev I, Nudnova M, Starikovskaya S and Starikovskii A Y 2012 Plasma decay in the afterglow of a high-voltage nanosecond discharge in air *Plasma Phys. Rep.* **38** 179–86

[45] Stancu G D, Kaddouri F, Lacoste D and Laux C 2010 Atmospheric pressure plasma diagnostics by OES, CRDS and TALIF *J. Phys. D: Appl. Phys.* **43** 124002